Traffic 2010; **11:** 440–454

doi:10.1111/j.1600-0854.2010.01040.x

Toolbox

Selective Visualization of Fluorescent Sterols in *Caenorhabditis elegans* by Bleach-Rate-Based Image Segmentation

Daniel Wüstner[1,*], Ane Landt Larsen[1], Nils J. Færgeman[1], Jonathan R. Brewer[2] and Daniel Sage[3]

[1]Department of Biochemistry and Molecular Biology
[2]MEMPHYS Center for Biomembrane Physics, Department of Chemistry and Physics, University of Southern Denmark, DK-5230 Odense M, Denmark
[3]Biomedical Imaging Group, Ecole Polytechnique Fédérale de Lausanne (EPFL), CH-1015 Lausanne, Switzerland
**Corresponding author: Daniel Wüstner, wuestner@bmb.sdu.dk*

The nematode *Caenorhabditis elegans* is a genetically tractable model organism to investigate sterol transport. *In vivo* imaging of the fluorescent sterol, dehydroergosterol (DHE), is challenged by *C. elegans*' high autofluorescence in the same spectral region as emission of DHE. We present a method to detect DHE selectively, based on its rapid bleaching kinetics compared to cellular autofluorescence. Worms were repeatedly imaged on an ultraviolet-sensitive wide field (UV-WF) microscope, and bleaching kinetics of DHE were fitted on a pixel-basis to mathematical models describing the intensity decay. Bleach-rate constants were determined for DHE *in vivo* and confirmed in model membranes. Using this method, we could detect enrichment of DHE in specific tissues like the nerve ring, the spermateca and oocytes. We confirm these results in *C. elegans* gut-granule-loss (glo) mutants with reduced autofluorescence and compare our method with three-photon excitation microscopy of sterol in selected tissues. Bleach-rate-based UV-WF imaging is a useful tool for genetic screening experiments on sterol transport, as exemplified by RNA interference against the rme-2 gene coding for the yolk receptor and for worm homologues of Niemann-Pick C disease proteins. Our approach is generally useful for identifying fluorescent probes in the presence of high cellular autofluorescence.

Key words: bleaching, cholesterol, dehydroergosterol, fluorescence, *in vivo* imaging, multiphoton microscopy, segmentation, transport

Received 5 October 2009, revised and accepted for publication 11 January 2010, uncorrected manuscript published online 12 January 2010

Metabolic diseases like atherosclerosis are the leading cause of death in the Western society. Stroke and coronary heart disease (CHD) are partially caused by cholesterol disposition in the arterial wall resulting in plaque formation and eventual plaque rupture, thrombosis and myocardial infarction (1,2). It is increasingly acknowledged that CHD is a complex disease with a strong genetic component (1). A major challenge is therefore to identify the key players of cellular sterol transport in a genetically tractable model organism. More than 60% of human disease genes have invertebrate orthologs, and the nematode *Caenorhabditis elegans* has been proven to be a good model for exploring the genetics of fat storage and lipid metabolism (3). *Caenorhabditis elegans* is auxotroph for sterols and easy to handle in genetic experiments. Moreover, several orthologs of human proteins being involved in intracellular cholesterol trafficking or intestinal absorption of sterols have been discovered in the nematode (4–9). This makes *C. elegans* an ideal model system for investigation of sterol metabolism and transport (10). A real challenge, however, represents the development of adequate experimental setups for characterization of sterol transport in *C. elegans*. The cholesterol-binding polyene filipin has been used to determine distribution of cholesterol in the nematode, but this approach suffered from severe limitations including sterol extraction during the experiment and limited access of the marker to all sterol-containing tissues (11,12). In a recent publication, Kurzchalia and colleagues have studied sterol distribution in living *C. elegans* using fluorescence imaging of the intrinsically fluorescent sterol dehydroergosterol (DHE) (12). DHE does not have a bulky reporter group and can be used by *C. elegans* as only sterol source (12,13). DHE resembles most closely ergosterol from which it differs only in having one additional double bond in the steroid nucleus making DHE slightly fluorescent in the ultraviolet (UV). We showed recently that DHE, like cholesterol or ergosterol, can induce the biologically relevant liquid-ordered phase in model membranes (14). Moreover, DHE supports growth of partially sterol-auxotroph mammalian cells and has the same intracellular distribution like cholesterol, as judged by fluorescence microscopy and biochemical assays (15–17). Several studies indicate that DHE has a somewhat lower capacity than cholesterol to order fatty acyl chains of phospholipids and thereby to condense lipid bilayers [reviewed in Ref. (13)]. Importantly, *C. elegans*, as a sterol-auxotroph organism, uses cholesterol as well as ergosterol as a sterol source (8,12,18,19). Despite the elegance of the study by Matyash et al. (2001) to follow

sterol trafficking by imaging DHE in nematodes, the authors could not satisfactorily discriminate between DHE's fluorescence emission (between 370 and 400 nm in membranes) and the high autofluorescence found in the same spectral region in *C. elegans* (12). In fact, it was shown by a spectrofluorimetric approach that age pigments create strong autofluorescence in nematodes with two characteristic intensity maxima (20). The first excitation/emission pair at 290/330 nm is mainly caused by cellular protein due to fluorescence of aromatic amino acids like tryptophan, while the second excitation/emission pair at 340/430 nm is due to age-associated advanced glycation end-products and lipofuscin (20). The latter proteins localize to lysosomal gut granules in *C. elegans*, making these structures highly fluorescent over a broad spectral range. Notably, excitation and emission maxima of DHE are at 330 nm and 380–410 nm, respectively, strongly overlapping with the autofluorescence of *C. elegans*. A method is therefore needed to discriminate between fluorescence emitted by the sterol compared to cellular autofluorescence generated by age pigments in the adult worms. We present a new approach based on the different bleaching kinetics of DHE and autofluorescent structures, to selectively detect DHE in living nematodes. By this method, we obtained new insight into sterol distribution in *C. elegans*. We also introduce *in vivo* three-photon microscopy of DHE and assess the suitability of this method for investigating sterol transport in living nematodes. The potential of the developed methods for genetic screening experiments to identify genes controlling sterol homeostasis in *C. elegans* is discussed. Finally, the relationship of our method to fluorescence lifetime imaging is explained.

Results

Assessment of different analysis methods for bleach-rate-based image segmentation

To demonstrate the principle behind our selective DHE imaging method, *C. elegans* were incubated with DHE/MCD for 3 days, such that the second generation grew to adult worms (12). Those worms show high fluorescence intensity in the oocytes, embryos and in the intestine when imaged in the UV channel of the microscope (Figure 1A). By repeatedly imaging the same field we realized that fluorescence in the oocytes decreased rapidly (arrows, Figure 1A), while the intensity in the intestine in the other half of the body remained almost constant. We showed previously that DHE bleaches rapidly in living mammalian cells as well as in model membranes (14,21,22). Thus, it is likely that the rapidly decreasing fluorescence stems from DHE, while the very slowly decaying intensity resembles autofluorescence. For two labelled regions of equal intensity, the difference in bleaching kinetics can be used to advantage in order to segment the image, as outlined in Figure 1B–F: repeated illumination results in a

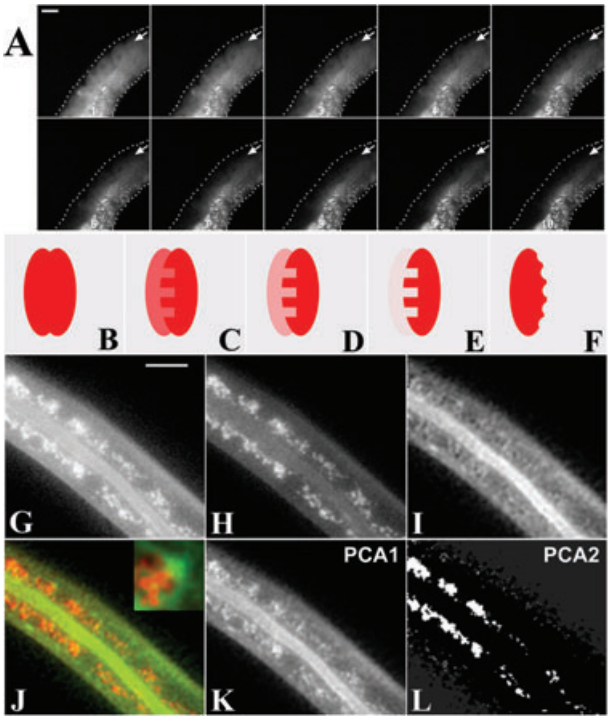

Figure 1: Separation of DHE-staining from autofluorescence by image subtraction. (A) DHE-stained adult *C. elegans* was repeatedly imaged on a UV-sensitive wide field microscope with 2 s acquisition time. Fluorescence decreased on the abdominal site, where oocytes and embryos containing DHE are located (arrows). In contrast, intestinal autofluorescence on the ventral site experienced almost no bleaching. (B–F) Principle of image subtraction: two overlapping fluorescent regions of comparable intensity (B) are repeatedly illuminated resulting in a strong fluorescence decay in the rapidly bleaching region (C–E), such that only the non-bleaching region remains (E). Subtracting the image in panel E from that in panel B gives only the rapidly bleaching region, shown in panel F. (G–L) example for DHE-stained L4-larvae of *C. elegans*. (G) 1st image, (H) 15th image of acquired bleach stack, (I) difference image (panel G minus panel H). (J) colour overlay with green and red corresponding to the 1st (G) and 15th (H) image of the stack. (K and L), PCA of panel G and H, with the two principle components named 'PCA1' and 'PCA2', respectively. Bar, 20 m.

bleach stack, where autofluorescence and DHE-labelled tissues bleach with their respective rates. The faster bleaching, DHE-containing region will likely experience rapid intensity decay to almost zero before significant bleaching of cellular autofluorescence takes place. Thus, our first strategy was to simply subtract the last image of a bleach stack from the first in order to obtain an image of the region containing the fast bleaching component, likely DHE. As shown in Figure 1G–L, this method works quite well: a nematode in the L2 larval stage contained fluorescence in gut granules as well as along the apical membrane of the intestine (Figure 1G). In the last image of the bleach stack, only fluorescing gut granules remained (Figure 1H). After subtracting the image in panel H from

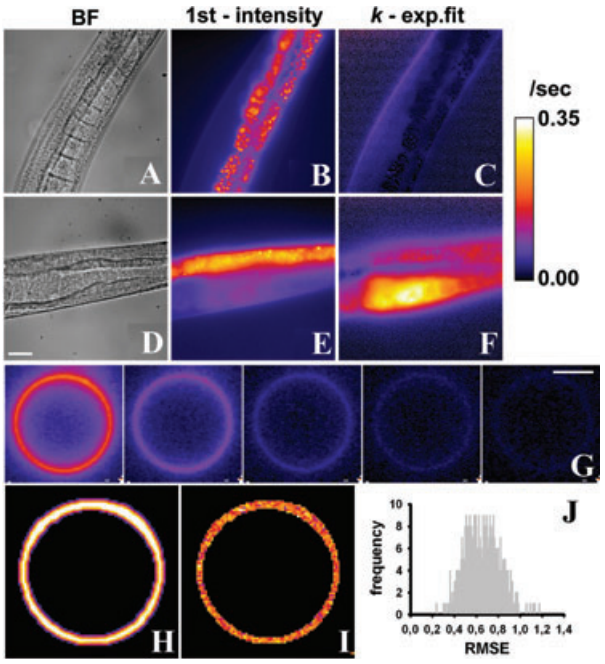

Figure 2: Pixel-wise kinetic fitting of the intensity decay caused by photobleaching. (A–F) Non-labelled (A–C) or DHE-labelled adult *C. elegans* (D–F) were repeatedly imaged as described in legend to Figure 1, above. Intensity decay in the resulting bleach stacks was fitted on a pixel-basis to a mono-exponential decay model, given in Eq. 2 of *Materials and methods* using the program PixBleach. (A, B) shows bright field (BF) images, while panels (B, E) shows the first acquired image of each bleach stack, named '1st-intensity'. (C, F) calculated rate-constant image expressing the rate constant $k(x,y)$ (inverse of time constant) of the bleaching process for each pixel position, x, y (named 'k – exp.fit'). Bar, 20 m. (G–J) GUV consisting of DPPC and 45 mol% DHE were imaged as described for *C. elegans*. G shows the first five acquired planes, (H) bleach-rate constant image shown in the same colour coding as above for *C. elegans* (range 0–0.35 s^{-1}). I and J, RMSE of the fit, as calculated by PixBleach, shown as image (I) or as histogram (J). Bar, 10 m.

the first acquired image in panel G, we obtain an image highlighting selectively the rapidly bleaching fluorescence in the apical membrane of intestinal cells (Figure 1I). This rapidly bleaching fluorescence resembles DHE. The colour overlay and the principal component analysis (PCA) of panels G and H in Figure 1 confirm that intestinal gut granules do not contain any rapidly bleaching sterol fluorescence.

By pixel-wise non-linear regression of a single-exponential decay model given in eqn 2, we were able to determine independently the bleach-rate constants of autofluorescence in non-labelled worms (Figure 2A–C) and of autofluorescence and DHE in nematodes labelled with the sterol (Figure 2D–F). To this end, we developed a plugin to the popular, Java-based image-analysis software ImageJ (NIH image, http://rsb.info.nih.gov/ij). This plugin named PixBleach performs a non-linear fit of different mathematical models describing the bleaching process to the experimental data. The user can choose a bleach model for a particular application including a single- and bi-exponential decay as well as a stretched exponential. In addition to calculating the bleach time-constant and amplitude image, our algorithm assess' the goodness of fit using the root mean square error (RMSE) and the chi-square value. The PixBleach plugin to ImageJ is available for download at http://bigwww.epfl.ch/algorithms/pixbleach/. Analysis of the acquired stacks with PixBleach revealed that fluorescence intensity bleaches at least sixfold faster in oocytes and embryos of DHE-stained nematodes than in autofluorescent gut granules of the intestine in both labelled and non-labelled worms (compare Figure 2C,F). For the example shown in Figure 2C, autofluorescence decayed with a characteristic rate constant of 0.03–0.048 s^{-1} with a standard deviation of typically 30% of the mean indicating some spatial heterogeneity in photobleaching kinetics of autofluorescent structures. Autofluorescence bleached slowest in gut granules (bleach-rate constant of $k_B = 0.031 \pm 0.011\ s^{-1}$) and slightly faster in epidermis and reproductive organs ($k_B = 0.048 \pm 0.014\ s^{-1}$). Typically, autofluorescence in gut granules bleached only by about 10–30% with the remaining intensity estimated as background fluorescence by the fitting procedure (see term 'B' in eqn 2, *Materials and methods*). Thus, a significant portion of the autofluorescent material in adult nematodes does not experience any photobleaching within the time course of continuous illumination required to bleach DHE completely. We found that DHE intensity decays with a bleach-rate constant in the range of 0.28–0.32 s^{-1} depending on the exact region one is looking at and the signal-to-noise ratio in this region. Fluorescence intensity in sterol-containing tissue on the ventral side of the worms, like gonades and embryos, decayed by 70–75% with the remaining intensity likely resembling autofluorescent background (Figure 2E,F). Due to the 6- to 10-fold faster bleaching of DHE than autofluorescence, we found no overlap of the distributions of the bleach-rate constants for labelled and non-labelled nematodes. In addition, regions with highest autofluorescence, like intestinal gut granules, experienced only partial bleaching by about 10–20% during the time course of the experiment. Thus, differences in bleaching kinetics are large enough to segment images of DHE-stained *C. elegans* and to discriminate the sterol probe from autofluorescence. Additional simulations confirm that varying bleaching kinetics of autofluorescence in a physicologically relevant range is without significant effect on the fluorescence intensity which can theoretically be collected by our imaging system from the rapidly bleaching DHE fluorophore (see Supporting Information Figure S9).

Importantly, we found comparable values of bleach-rate constants for DHE in living worms and in model membranes: the fluorescent sterol bleached with a single rate constant of $k_B = 0.31 \pm 0.02\ s^{-1}$ in giant unilamellar vesicles (GUV) consisting of dipalmitoyl-phosphatidylcholine

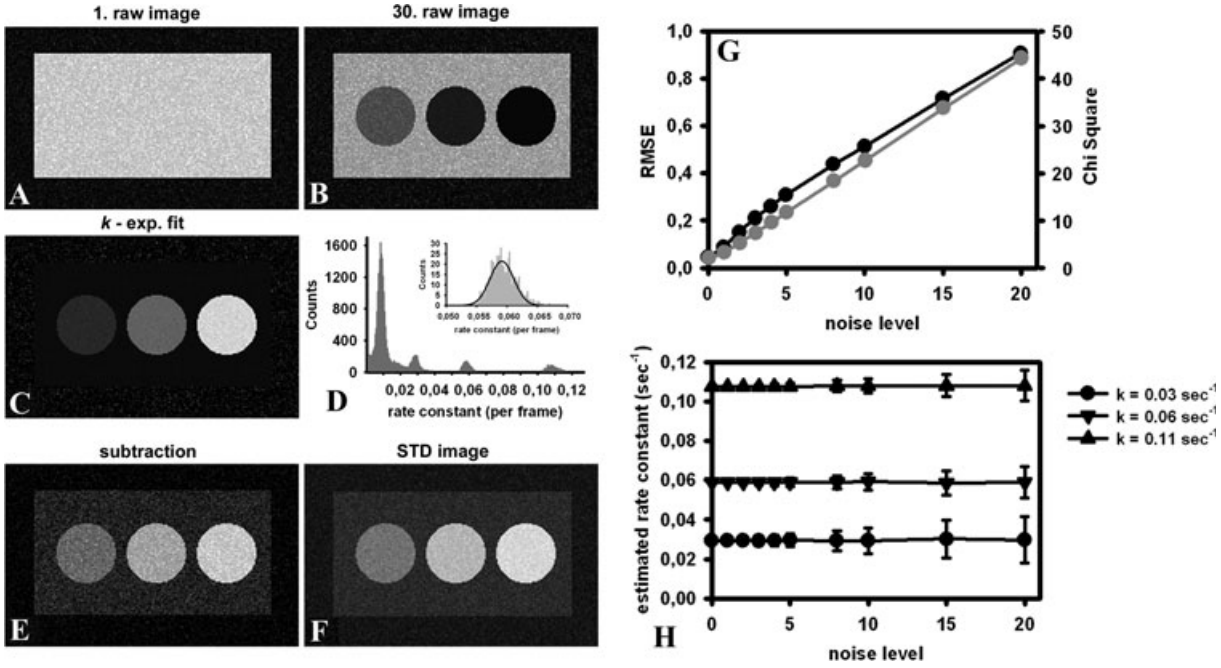

Figure 3: Assessment of bleach-rate-based image segmentation methods. A synthetic image stack was generated with tools in ImageJ containing a rectangle with a mean intensity of 190 and a bleach rate 0.01 s^{-1} in an 8-bit image on non-bleaching background (intensity zero) and three circles having the same intensity value of 190 but differing bleach rates of 0.03, 0.06 and 0.11 s^{-1}, respectively (from left to right). (A, B) 1st and 30th image of this synthetic bleach stack named 'raw image'; (C, D) calculated rate-constant image expressing the rate constant $k(x,y)$ (inverse of time constant) of the bleaching process for each pixel position, x, y as image (named 'k – exp. fit', panel C) or as histogram (D). Inset to D, histogram (grey bars) and Gaussian fit to the estimated rate constants within the middle circle giving a mean and standard deviation of 0.05766 ± 0.00195 compared to the theoretical value of 0.06 (see above). (E) result of subtracting the 30th from the 1st raw image (i.e. panel A minus panel B). (F) Result of calculating the standard deviation ('STD') of the raw bleach image stacks according to eqn 7 in *Materials and methods*. (G) goodness of fit using a mono-exponential model in PixBleach to image stacks as shown in panel A, B with differing added Gaussian noise levels. PixBleach calculates the RMSE (black curve, left axis) and chi-square value (grey curve, right axis) of the fit. (H) accuracy of parameter estimation by PixBleach for the three circles shown in panel A–C, as function of image noise expressed as mean ± SD.

(DPPC) and 45 mol% DHE (Figure 2H). From the RMSE (Figure 2I,J) and chi-square images (not shown), we conclude that a mono-exponential model accurately describes the bleaching kinetics of DHE (see also Supporting Information Figure S7). The same was found for DHE-labelled nematodes. Regression of the bi-exponential model, given by eqn 4 in *Materials and methods*, provided worse results (not shown). This is probably due to increased impact of image noise when fitting the two additional parameters to the same data set (23). We also tested whether photobleaching of DHE can be described by a linear superposition of mono-exponential decays using a stretched-exponential function (see eqn 3 *Materials and methods*). Fitting the stretched exponential gave a heterogeneity factor of $h = 1$ for GUV and $h = 0.95 - 1.05$ for DHE-containing worms. This parameter is a direct measure of the width of the bleach time constant distribution, with $h = 1$ being identical to the mono-exponential model (compare eqns 2 and 3 in *Materials and methods*). Thus, bleaching of DHE can be accurately described by a single mono-exponential decay function for each individual pixel position. This was found for DHE in GUV model membranes and in living *C. elegans* (see above) as well as in DHE-labelled mammalian cells (see Supporting Information Figure S5).

To test various bleach-rate-based image segmentation methods systematically, we generated synthetic images with varying known bleach rates. As an example of such tests, Figure 3A,B shows a rectangle with a mean intensity of 190 and a bleach rate constant of 0.01 s^{-1} in an 8-bit image on non-bleaching background and three circles having the same intensity but differing bleach-rate constants of 0.03, 0.06 and 0.11 s^{-1}, respectively (from left to right). Since the intensity was the same for all regions (with some added Gaussian noise) no contrast can be found within the rectangle in the first image of the synthetic bleach stack (Figure 3A). In the course of bleaching, the three circles become visible, due to the fact that they bleach faster than the surrounding rectangle (see Figure 3B for the last, 30th, image of this synthetic bleach stack). Additional illustrations are found in Supporting Information Figure S1. Our pixel-wise fitting routine implemented in the PixBleach plugin nicely segments the

image based on the differing bleach rates and additionally obtains accurate estimates for the individual bleach-rate constants (Figure 3C,D). This is shown in the histogram of the bleach-rate image obtained from the fit of eqn 2 to the data (Figure 3D). A simulation of the synthetic bleach stack with different levels of Gaussian noise and fitting of the intensity decay in the stacks demonstrates that PixBleach gives accurate estimates for the bleach-rate constant over a large range of noise levels (Figure 3H). This accuracy requires only that the mean intensity of the bleaching regions is high enough.

Two other methods of bleach-kinetics-based image segmentation, i.e. image subtraction and calculation of a standard deviation image ('STD image') using tools in ImageJ, provided very good segmentation of the images as well (Figure 3E,F). A fourth method for segmentation of DHE images based on the ratio of the two images provided less contrast in our application (see Supporting Information Figure S2) (24). A particular advantage of the simple image subtraction method outlined in Figure 1 becomes apparent in case of specimen movement during the acquisition of a bleach stack. We found that despite treatment of nematodes with anaesthetics right before imaging, occasionally the worms moved slightly during image acquisition. This can result in artefacts in the post-processing for image segmentation. One can correct for this movement by spatial image registration (see *Materials and methods*). In contrast to pixel-wise fitting and calculation of an STD image, the simple image subtraction method requires only two spatially registered planes, but not the whole stack to be spatially aligned. Thus, in the rare case of specimen movement, we chose to use the image subtraction method after spatially registering the first and last planes of the bleach stack. Pixel-wise bleach-rate fitting, on the other hand, offers the advantage to obtain numbers for the bleach-rate constants of the fluorophore per second, which can be used as a fingerprint to distinguish DHE from autofluorescence. Thus, our method makes it obsolete to compare DHE-stained and non-stained worms in every single experiment. This was clearly required in an earlier study, since intensity of cellular autofluorescence can differ dramatically between different worms and developmental stages (12). The pixel-wise bleach-rate fitting analysis demonstrates also that the time hierarchy of bleaching rates satisfies the assumption of considering the autofluorescence as constant, as required for the image subtraction method and for good contrast in the STD images. This is confirmed by additional simulations (see Supporting Information Figure S9). We assessed independently using synthetic images, how sensitive the fitting accuracy of PixBleach is for varying noise levels in the image bleach stack. There was a linear relationship between the noise level in the images and the RMSE as well as the chi-square value (Figure 3G). Accordingly, for higher noise levels at the same signal strength, the quality of the reconstruction suffers dramatically. On the other hand, the accuracy of the estimation of bleach-rate constants is relatively insensitive against image noise for a given image intensity, i.e. signal, as shown in Figure 3H. We determined independently using a parameter sensitivity analysis that the accuracy of the fit depends mostly on the amount of DHE in a particular region, with low amounts being fitted less accurately (see Supporting Information Figure S3). Moreover, blurring of images by out-of-focus fluorescence, as it is typically found in wide field microscopy, degrades also the contrast in the bleach-rate images (see Supporting Information Figure S4).

In the case of very heterogeneous DHE intensity, the bleach-rate image differed from the difference and STD image, respectively (not shown). This is because image contrast generated by the latter two methods but not by pixel-wise bleach-rate fitting is sensitive to the intensity in the first frame of a bleach stack (corresponding to the amplitude in a single-exponential fit). In other words, computational estimates of the bleach time constant, or equivalently the bleach-rate constant, are insensitive to varying degrees of accumulation of DHE in certain tissues. The PixBleach plugin offers the possibility to assess in a pre-processing step, which structures in an image stack show enough bleaching mediated intensity decay to be worth fitting by the applied model. This minimal decay from the first to the last frame at a specific position P in the image stack is set by a user-defined threshold, so the model does not optimize at P, if the decay is below this threshold. Accordingly, one can select – before applying PixBleach – approximately the sterol-containing regions in a specimen using this option. This is exemplified in Figure 4, where autofluorescence in certain gut granules highlighted by a rectangle decays by less than 10 units between the first (Figure 4A) and 30th frame (Figure 4B) in a 12-bit image with 4096 intensity units total. Setting the minimal decay threshold to 10 units allows the user to highlight only the bleaching features (Figure 4C). By setting the minimal decay threshold to values above the characteristic bleach-rate range of cellular autofluorescence, the sterol distribution can be directly inferred from the amplitude image of the bleaching fraction (Figure 4D). This offers the additional advantage that areas of strongly differing DHE intensity can easily be distinguished from each other as well as from cellular autofluorescence, since the amplitude image of the bleach-rate-thresholded stack is a measure of DHE intensity. The time-constant image alone would not provide any contrast between two regions containing different amounts of DHE, since this parameter is not sensitive for differing intensities (Figure 4F).

We illustrate this principle again on synthetic images as shown in Figure 4G–L: three circles of intensity $I = 200$, $I = 100$ and $I = 50$ (from left to right) on a rectangular region with $I = 100$. All circles bleach with the same rate constant of $k = 0.31\ s^{-1}$, while the rectangle bleaches with a rate constant of $k = 0.01\ s^{-1}$. Without minimal decay option, the amplitude image does not provide

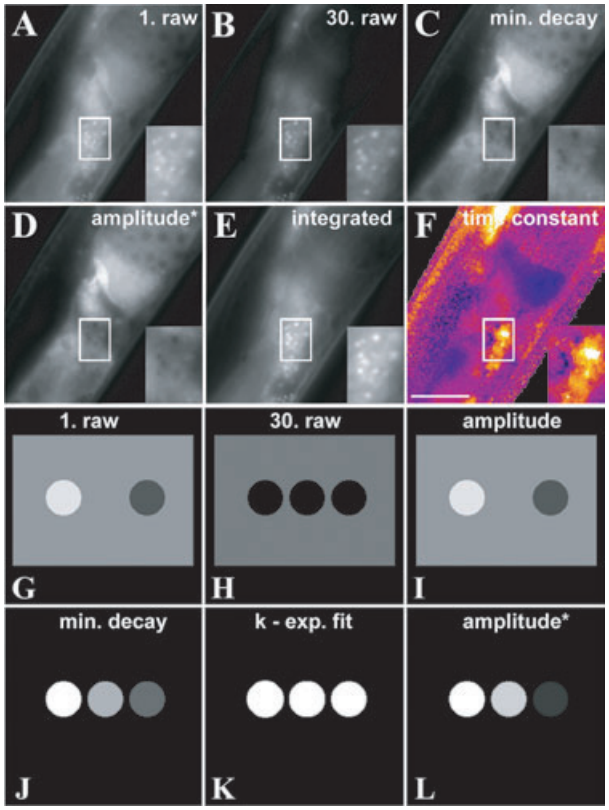

Figure 4: Improved detection of DHE in the presence of autofluorescence using decay-thresholding. (A–F) adult nematodes labelled with DHE were imaged and as described in legend to Figure 1, above. (A, B) first and 30th raw image, (C) minimal decay ('min.decay') set to 10 intensity units shows only those regions in the image experiencing at least an intensity decay of 10. Only these regions are fitted by PixBleach to a mono-exponential decay model, explaining the term decay-thresholding as pre-processing step. (D) calculated amplitude image of this fit (named 'amplitude*') highlighting DHE-containing regions. (E, F) integrated intensity and time-constant image as obtained from the fit for the whole bleach stack. (G–L) synthetic images illustrating the principle of the MinDecay option: (G, H) first and 30th plane of a synthetic image stack generated as described in legend to Figure 3 but with minor differences: three circles of intensity $I = 200$, $I = 100$ and $I = 50$ (from left to right) on a rectangular region with $I = 100$. All circles bleach with the same rate constant of $k = 0.31\ s^{-1}$, while the rectangle bleaches with a rate constant of $k = 0.01\ s^{-1}$. Without decay-thresholding, the calculated amplitude image is identical to the 1st raw image (I, compare panel G). (J) minimal decay threshold set to 30 units. (K, L) rate-constant image ('k – exp.fit') and amplitude image of the fit after applying the min. decay threshold. Only in panels J ('min. decay') and L ('amplitude*') the three bleaching circles can be discriminated. See text for further explanations. Bar, 20 m.

contrast between the second circle and the rectangular background region (Figure 4I). Setting the minimal decay to a value of 30, the rectangular region is excluded from the fitting procedure, where the total decay does not exceed a value of 15, in this particular example (Figure 4J). Thus, applying the minimal decay option before fitting provides an amplitude image for the three circles which all show a decay being larger than 30 from the first to the last image of the stack (Figure 4L). In contrast, the time constant, or equivalently, the rate-constant image does not allow for distinguishing between the three circles, since they all bleach with the same rate constant (Figure 4K). In summary, the minimal decay option is a convenient way to threshold the bleach stacks based on the experienced intensity decay from the first to the last frame. By this thresholding PixBleach confines the pixel-wise fitting to areas experiencing an intensity decay larger than the set threshold. By setting the threshold above the intensity decay of typical autofluorescent structures, we can limit the fit to pixels containing DHE. From the amplitude image obtained in this manner (named 'amplitude*'), we can detect regions of differing DHE intensity in the various tissues of *C. elegans*. Varying DHE intensity will not generate contrast in the time-constant image, due to the homogeneous bleaching characteristics of DHE. Note that the threshold defined here applies to the experienced intensity decay due to photobleaching of the fluorescent structures. This is in contrast to the more common intensity thresholding, where images are segmented based on intensity differences in a single frame (22). We found also that the amplitude* image is less sensitive to image blurring than the time constant or bleach-rate image, and is therefore better suited to highlight DHE in case of strong out-of-focus fluorescence (see Supporting Information Figure S4). Moreover, the amplitude* image is directly related to the intensity emitted by DHE in the sample and thereby to the amount of fluorescent sterol in various tissues of the nematodes (25).

For large differences in bleaching kinetics of probe fluorescence versus autofluorescence with no overlap between the respective distributions of time constants, one can quite exactly infer the relative fluorophore distribution from the minimal decay image. Under these circumstances, the minimal decay image is very similar to the amplitude* image (compare Figure 4C,D and 4J,L) and resembles a thresholded difference image from our simple image subtraction method (see above and Figure 1, and (ii) in *Materials and methods*).

Another advantage of pixel-wise bleach-rate fitting of decay data to a mathematical model is the possibility to quantify time-integrated emission of UV fluorescence in selected tissues (both autofluorescence and DHE). Hirschfeld has shown that the time-integrated fluorescence signal is independent of the quantum yield of the fluorophore and represents the total intensity emitted by the fluorophores before complete photodestruction has taken place (25). The time-integrated fluorescence of DHE-stained worms differs dramatically from the calculated amplitude image (Figure 4D,E). Thus, due to the large differences in bleach-rate constants of DHE and autofluorescence, the rapidly bleaching DHE fluorescence is strongly underrepresented in the time-integrated image.

Intestinal gut granules have high, slowly bleaching autofluorescence in the same spectral region as emission of DHE in the worms, and this gives the largest contribution to the time-integrated signal of fluorescence emission (26). Accordingly, simple extension of the acquisition time will not provide better images of DHE distribution, since mostly autofluorescence will be collected. A theoretical analysis where we plot the acquired intensity as function of acquisition time makes this more plausible: even in situations where autofluorescence intensity is lower than rapidly bleaching DHE intensity, extension of the acquisition time would increasingly sample the slowly bleaching autofluorescent background (see Supporting Information Figure S8).

Differences between amplitude and time-integrated images of DHE-stained *C. elegans* could theoretically also be caused by local self-quenching of fluorescent sterol, since only time-integrated fluorescence is independent of quantum yield (25,26). In fact, DHE has been reported to self-quench in small unilamellar vesicles made of 1-palmitoyl-2-oleoylphosphatidylcholine (POPC) (27). Concentration-dependent self-quenching of a fluorophore can be detected by decreased fluorescence intensity and slowed bleaching kinetics compared to membranes with lower fluorophore concentration [see eqn 1 in *Discussion* and (25,26)]. We measured the bleaching kinetics of DHE in GUV made of DPPC and 30 mol% DHE and got the same rate constants as those in Figure 2 for DPPC containing 45 mol% DHE [see figure 3D,E in Ref (14)]. Moreover, we calculated the ratio of amplitude and integrated image for various GUVs and found no evidence for local differences in quantum yield (see Supporting Information Figure S7). Thus, we can rule out that potential concentration self-quenching of DHE in lipid membranes affects our analysis.

Tissue distribution of DHE in wild-type and gut-granule-loss mutant *C. elegans*

By all three method described above, we could detect DHE in the pharynx, in head neurons and the excretory gland cells (Figure 5A–D), in spermatids and the spermathecal valve (Figure 5E,E'), in embryos (Figure 5F) and in (proximal) oocytes (Figure 5G) in adult *C. elegans*. We also demonstrate compartmentalization of sterol in the oocytes and embryos with DHE-containing vesicles in the cytoplasm close to the plasma membrane of those cells (inset of Figure 5F,G with inverted intensity values for better visual contrast). Since these vesicles bleach rapidly with a rate constant typical for DHE and become visible only after applying our bleach-rate-based image segmentation method, we can be sure that they contain large amounts of the fluorescent sterol. To confirm the suitability of WF-UV bleach-rate microscopy for *in vivo* imaging of sterol, we assessed the distribution of DHE in mutant worms with reduced autofluorescence. Nematodes having mutations in genes

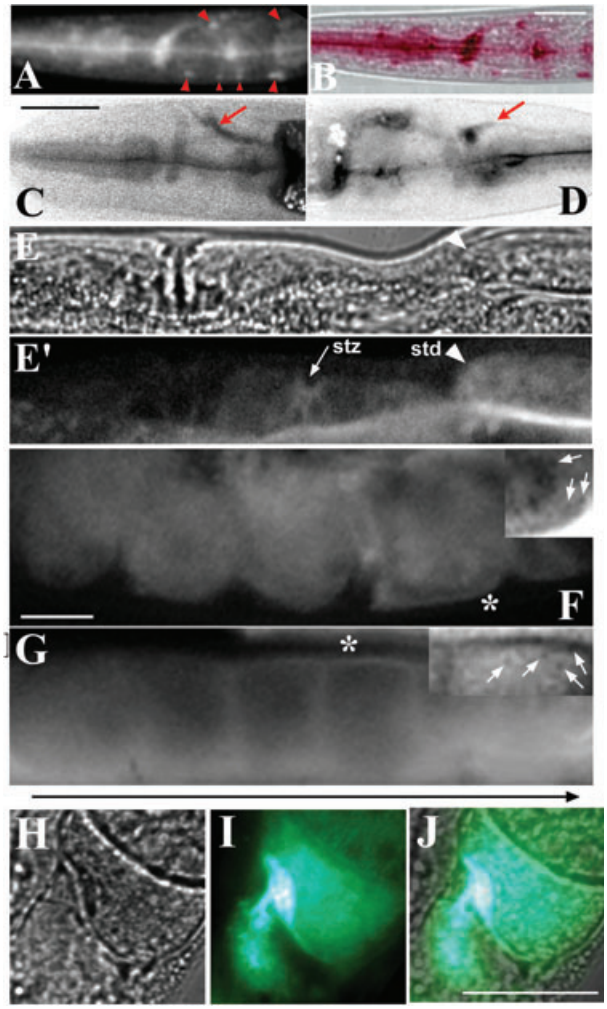

Figure 5: DHE accumulates in specific tissues in adult *C. elegans* as revealed by various methods of bleach-rate-based image segmentation. Nematodes were labelled with DHE and imaged as described in legend to Figure 1, above. DHE was detected in ganglions of the head regions (arrowheads, A); B, colour overlay to panel A, showing DHE fluorescence in red above the bright field image of a worm head. Sterol enrichment was also found in the olfactory bulb (arrows), images in panel C, D (grey values were inverted for better contrast); in the reproductive organs like spermatids ('std') and spermatecal valve ('stz', E, E'), embryos (F) and oocytes (G). In embryos and oocytes DHE was detected in cytoplasmic vesicles (arrows in insets, F and G). H–J, prominent sterol accumulation in the spermatecal valve and in adjacent embryos as detected by bleach-rate imaging of DHE. H, bright field image, I, DHE image, J, overlay. Bar, 20 m. The black arrow in panel G indicates the direction of oocyte maturation. Bar, 20 m.

involved in the biosynthesis of gut granules show a glo (gut granule loss) phenotype, characterized by loss or mislocalization of birefringent and autofluorescent material into the intestinal lumen of embryos and loss of adult autofluorescent gut granules (5,6). We used three glo-mutants: the mutant *glo-1* is defective for a Rab

GTPase, homologous to mammalian Rab38, located in the membranes of intestinal gut granules (5). The mutant *glo-4* misses a functional putative guanine nucleotide exchange factor for *glo-1* (5). *Caenorhabditis elegans* with a loss of function in *pgp-2* encoding for an ATP-binding cassette transporter also lack gut granules (6). Mutant larvae and adult worms for all three genes have in common that they lack birefringent and autofluorescent gut granules and mislocalize gut granule contents including triacylglycerides into the intestinal lumen during embryogenesis (5,6). We confirmed the absence of intact birefringent gut granules by staining worms with NileRed (see Supporting Information Figure S6) (5). Adult glo-mutants, *glo-1*, *glo-4* and *pgp-2*, had strongly reduced intestinal autofluorescence recorded in the UV/DHE channel of the microscope compared to wild-type (N2) worms, as exemplified for adult glo-4 nematodes in Figure 6A–F. The first frame of the bleach stack (termed '1st raw' in Figure 6A,D) contains autofluorescence as well as DHE fluorescence. A map of DHE-containing tissues was provided by the amplitude* image obtained after applying pixel-wise bleach-rate fitting with PixBleach to image stacks of wild-type (Figure 6A) and *glo-4* mutant worms (Figure 6D). The background intensity estimated from the parameter '*B*' in the mono-exponential model of PixBleach (eqn 2, *Materials and methods*) highlighted specifically the autofluorescence in N2 (Figure 6B) and *glo-4* mutant nematodes (Figure 6E). We verified independently that this background estimate resembles autofluorescence: in *glo*-mutant worms the 'B-map' obtained from the fit of data using PixBleach visualized exclusively residual autofluorescence in the eggshell and gave identical distribution and intensity values as found for autofluorescence in non-stained glo-mutant worms (not shown). Thus, our method clearly separates DHE-staining from autofluorescence and further establishes that *glo*-mutant worms have strongly reduced intestinal autofluorescence compared to wild-type animals. The DHE map given by the amplitude* image reveals that both, the wild-type worms and the glo-mutants, have DHE accumulated in the oocytes, especially the most proximal one, located right next to the spermatheca, which also had very high fluorescence from DHE (Figure 6G–J'). The embryos inside the uterus were also labelled (Figure 6G–J'), and DHE was detected in head neurons and in the pharynx in all glo-mutants (not shown, but see Figure 5 for wild type). Quantification of DHE intensity from the amplitude* image of adult *pgp2*-worms labelled with DHE revealed that sterol accumulation was highest in the spermatecal valve (stz) (set to 100%) followed by the embryos (55.4 ± 3.2% of stz), proximal oocytes (51.9 ± 7.1% of stz), distal oocytes (51.9 ± 7.1% of stz) and finally the body cavity (10.9 ± 2.1% of stz). Similar values were found for wild-type animals (not shown). When the nematodes obtained sterol from DHE-containing bacteria instead, the same sterol distribution was found in wild-type and glo-mutant worms. The labelling intensity of the worms, however, was lower with this method (about 50% of that obtained by labelling worms with DHE via cyclodextrin complexes). The bleach-rate constants measured from the pixel-wise fitting of the intensity decay to the mono-exponential model using PixBleach were identical for wild-type and glo-mutant worms in DHE-containing regions (not shown). Occasionally, large accumulations of DHE-containing vesicular structures were detected in the intestine of glo-mutant worms, as exemplified for *glo4*-mutant worms in Figure 6K,L. In these animals, sterol accumulation in the intestine exceeded that observed in the spermatecal valve, as inferred from the corresponding amplitude* image. The reason for this pronounced intestinal DHE accumulation in glo-mutant worms and the nature of the sterol-enriched vesicles remains to be clarified.

Potential of three-photon excitation microscopy for imaging of DHE in *C. elegans*

An alternative approach for visualizing DHE is three-photon excitation (3P) microscopy, as shown for imaging of DHE in living fibroblasts with an excitation wavelength of 900–930 nm (28–30). Multiphoton excitation microscopy has an intrinsic sectioning capability due to the non-linear (quadratic for two-photon or cubic for 3P microscopy) dependence of excitation probability on excitation intensity (31). Due to the use of infrared lasers, high tissue penetration of the excitation beam enables imaging of a thick biological specimen. Thus, one would expect that this technique is very suitable for *in vivo* sterol imaging. We found, however, that the sterol distribution could not be assessed in wild-type *C. elegans* by 3P microscopy due to the overwhelming intestinal autofluorescence (not shown). Glo-mutant worms with reduced intestinal autofluorescence should be a good model system for studying sterol transport by 3P excitation. To test this, DHE-stained or non-labelled *pgp2*-worms were imaged using 3P excitation microscopy with identical settings. We observed reasonable fluorescence in the non-stained worms in the intestine as well as in the embryos (Figure 7A). This is most likely due to remaining gut autofluorescence as well as due to collagen and other autofluorescent structural proteins in the extracellular matrix of connective tissue of the worms (32). DHE-labelled worms had about twice the intensity in both tissues, but this was quite variable. Direct comparison of bleach-rate-based imaging in the WF-UV microscope with imaging by our 3P system shows that 3P microscopy detected high fluorescence intensity also in regions lacking DHE, like the eggshell as well as the body cavity (Figure 7B,C). Thus, 3P microscopy of DHE *per se* is not able to distinguish autofluorescence from intensity of the fluorescent sterol, and prior-knowledge from WF-UV microscopy of DHE is required to highlight the DHE-containing tissue. With such knowledge, 3P excitation generates high-contrast three-dimensional images of DHE in *C. elegans* mutants with reduced autofluorescence. The latter is demonstrated for the embryos in the uterus and the spermathecal valve

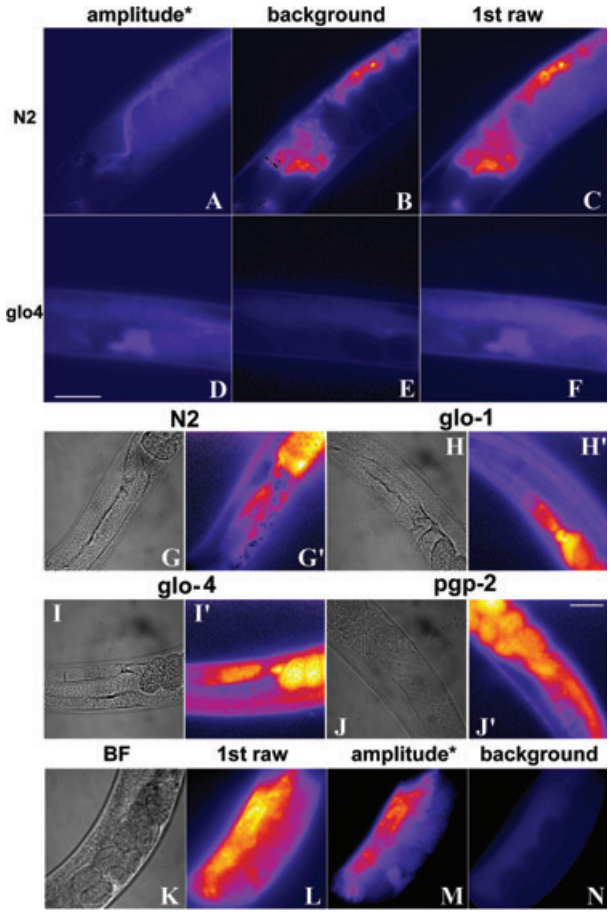

Figure 6: Distribution of DHE in glo-mutant worms and in response to RNAi against the yolk receptor. Wild-type and gut-granule-loss (glo) mutant worms were labelled with DHE and imaged as described in legend to Figure 1, above. A–F, bleach-rate image of wild-type ('N2', A–C) and glo-4 mutant worms ('glo4', D–F) showing the first acquired image of the bleach stack ('1st raw', C, F) as well as the amplitude* image resembling DHE fluorescence ('amplitude*', A, D) and the background image resembling autofluorescence ('background', B, E) as obtained from the mono-exponential pixel-wise fit to data using the PixBleach plugin to ImageJ. (G'–J') amplitude* image showing DHE distribution in wild-type (G') and glo-mutant worms ('glo1', H'; 'glo4', I' and 'pgp2', J'). (G, H, I, J) corresponding bright field images. (K–M) DHE-stained adult glo-4 nematode with high-granular intestinal sterol enrichment. (K) bright field image; (L) amplitude* image and (M) rate-constant image. Images (A-F) and (G-N) are shown with identical intensity scaling (red = high, blue = low intensity, respectively). Bar, 20 m.

of adult *pgp2*-nematodes (Figure 7D–F, arrows; compare Figure 5F,J). In summary, bleach-rate-based WF-UV microscopy of DHE in *C. elegans* can be complemented with 3P excitation microscopy, which due to its sectioning capability can provide additional information about sterol distribution. Overall, our bleach-rate-based WF-UV microscopy approach is the technique of choice for *in vivo* sterol imaging.

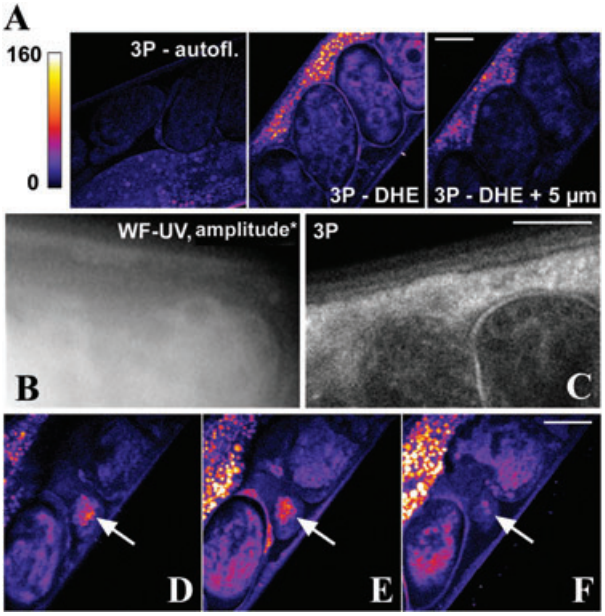

Figure 7: Comparison of multiphoton microscopy with bleach-rate-based imaging of DHE in pgp2-mutant worms. Gut-granule-loss (glo) pgp-2 mutant worms were labelled with DHE as described in legend to Figure 1, above, and imaged on a UV-sensitive wide field microscope (B) or on a multiphoton microscope (A, C–F) by a three-photon excitation process. (A) comparison of autofluorescence in non-stained pgp2-mutant worms (left panel) with DHE intensity in labelled pgp2 knock-out nematodes (A, middle and right panel). Images were scaled identically and the colour bar represents intensity. Embryos and epidermis of DHE-stained pgp2-worms as imaged by bleach-rate-based UV-sensitive widefield microscopy (B) or by three-photon excitation (C). Note strong autofluorescence in the egg shell and in connective tissue underneath the epidermis, as seen by multiphoton microscopy (C). (D–F) three planes being acquired 1 m apart along the optical *z*-axis in the multiphoton microscope, showing enrichment of DHE in the spermatecal valve (arrows). See text for further explanations. Bar, 20 m.

Bleach-rate imaging and RNAi for detection of genes regulating sterol transport

To assess the potential of our imaging approach, we disturbed intracellular cholesterol trafficking in *C. elegans* using RNA interference (RNAi) against the gene coding for the yolk receptor RME-2 in *pgp2*-mutant worms. Mutant worms lacking functional RME-2 have been shown to be unable to import yolk-protein-bound sterols into oocytes (12). We can confirm this result by our bleach-rate-based UV-WF imaging approach: rapidly bleaching intensity of DHE was found in the body cavity but not in oocytes of *pgp-2* mutant worms treated with dsRNA against the yolk receptor RME-2 (Figure 8C,D). This is in contrast to control *pgp-2* worms grown in the presence of the empty L440-vector (Figure 8A,D; see *Materials and methods*). Quantification of DHE intensity from the amplitude* image showed that sterol content in the body cavity of pgp-2 control nemtatodes never exceeded 20% of that found in (proximal oocytes). In contrast, in *pgp-2*

mutant worms with silenced rme-2 gene, DHE in the body cavity was at least 200% of that found in oocytes.

Niemann-Pick type C (NPC) disease is an autosomal recessive neurodegenerative disorder, where unesterified cholesterol accumulates in abnormal lysosome-like organelles in mammalian cells [46, 47]. Ninety-five percent of mutations causing NPC disease in humans affect the gene encoding NPC1, a large 1278-amino acid polytopic membrane protein being localized to the limiting membrane of late endosomes and lysosomes (33). NPC1 is thought to be involved in the redistribution of cholesterol after endocytosis of LDL-particles. The *C. elegans* genes *ncr-1* and *ncr-2* (NPC1 related genes) are homologous to the human *npc1* gene (9). The expression pattern of *ncr-1* coincides with the cholesterol distribution in *C. elegans* reported by Matyash et al. (12), while expression of *ncr-2* is limited to the XXXL/R neurons and the somatic gonad (7,12). These results led the authors conclude that *ncr-1* might be involved in cholesterol trafficking while *ncr-2* could function mainly in dauer formation (7,9). We directly addressed the question, whether *ncr-1* or *ncr-2* play a role in sterol trafficking in *C. elegans* by silencing the respective gene and determining the distribution of DHE using bleach-rate-based image segmentation in *pgp-2* worms (Figure 8E–H). The sterol distribution was very similar in control nematodes and in worms with silenced *ncr-1* or *ncr-2* genes. Down regulation of *ncr-1* by RNAi resulted occasionally in some DHE fluorescence in the body cavity adjacent to sterol-containing embryos (compare Figure 8E,F and Figure 8G,H). We conclude that worm *ncr-1* and *ncr-2* do not play a significant role in sterol trafficking between various tissues in *C. elegans*. Changes of intra-organelle sterol trafficking in some cells as a consequence of the gene silencing cannot be ruled out by our analysis. The reported hypersensitivity of the *ncr-1* mutant to cholesterol deprivation might alternatively be caused by defective steroid hormone processing or metabolism of the sterol precursor.

Discussion

We developed a technique to detect the intrinsically fluorescent sterol DHE in the presence of high autofluorescence in the genetic model organism *C. elegans*. The method is based on the rapid bleaching of DHE, and we developed software to automatically detect sterol in tissues by bleach-rate imaging. Photobleaching is the photochemical degradation of a fluorophore from the excited singlet or triplet state with bleached molecules being removed irreversibly from the excitation/emission photocycle. The rate of this light-induced degradation is characteristic for each fluorescent molecule. It can be used to co-detect and discriminate fluorophores of similar spectral characteristics (either various introduced fluorescence labels or label and autofluorescence). Another method to discriminate between various fluorophores of the same colour is fluorescence lifetime imaging. For example, various fluorophores with overlapping excitation and emission spectra but differing radiative lifetime of their excited state, τ_F, could be distinguished in living cells and tissue (23). However, this method relies on sophisticated imaging equipment not available in all cell biological laboratories.

There have been earlier attempts in mammalian cells to use pixel-wise differences in bleaching kinetics for discriminating between various fluorescent probes of the same colour (24,34–36). We found that the image processing used to discern various fluorophores based on differing bleaching kinetics in methods like bleach ratio imaging does not generate as good contrast as our approach (see above and Supporting Information Figure S2) (24). Moreover, pixel-wise fitting of mathematical models to the recorded intensity decay provides numbers for bleach-rate constants and allows for quantitative assessment of fluorophore distribution, in contrast to these earlier methods. Knowing the spatial distribution of bleach-rate constants provides complementary information to intensity, colour and lifetime of a given fluorophore. In fact, by analysing a mono-exponential bleaching process, Hirschfeld obtained a very simple relation between the bleach time constant of the average molecule in a normal distributed ensemble, τ_B, and the radiative fluorescence lifetime, τ_F (25):

$$\frac{1}{\tau_B} = k_B = \frac{\tau_F \cdot Q_F}{\tau_E \cdot \tau_R} \quad (1)$$

where, Q_F is the fluorescence quantum efficiency, τ_E the mean interval between successive molecular excitation events and τ_R the mean photodegradation time constant of the excited molecule.

Thus, assuming a homogeneous intracellular distribution of bleaching agents, like molecular oxygen, changes in fluorescence lifetime and/or quantum yield should be detectable as differences in bleach-rate constants, k_B. With our method of pixel-wise bleach-rate fitting, the measured bleach parameters can be compared between different labelled specimens. Interestingly, we observed the same distribution of bleach-rate constants of DHE in model membranes, mammalian cells and *C. elegans*. Since the lipid composition differs between model and cell membranes, it can be concluded that DHE's quantum yield is rather insensitive to changes in the local environment of the fluorescent sterol. This is confirmed by fluorescence lifetime measurements of DHE in various organic solvents; Smutzer et al. reported very little change in the fluorescence lifetime, τ_F, with respect to solvent and only minor alterations in τ_F for DHE in vesicles above the phase transition of the phospholipids (37). Several authors reported two lifetime components for DHE, but with one dominating component contributing by over 90% to total decay (37,38), while others found a mono-exponential lifetime decay (39). This is in good agreement with our observation of a mono-exponential bleaching process of DHE in model and cell membranes.

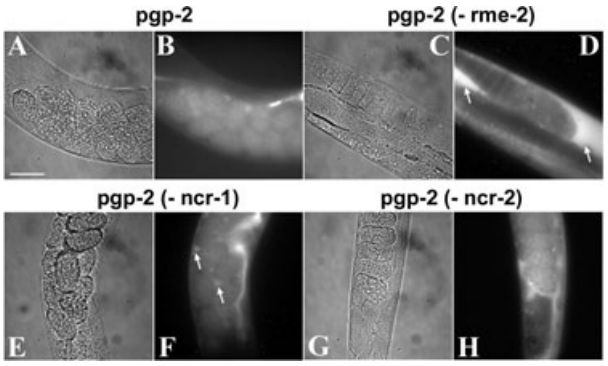

Figure 8: Bleach-rate-based imaging of DHE combined with RNA interference. Gut-granule-loss (glo) pgp-2 mutant worms, synchronized in the L4-larval stage were fed with bacteria containing either the empty L4440 vector (A, B); dsRNA against the rme-2 gene (C, D), the ncr-1 gene (E, F) or the ncr-2 gene, respectively (G, H). Worms were labelled with DHE and imaged on a UV-sensitive wide field microscope as described in legend to Figure 1, above. Bleach stacks were fitted to a mono-expoential function implemented in PixBleach, and the amplitude* image highlighting sterol distribution is shown (B, D, F, H). Arrows indicate sites of abnormal sterol enrichment (in the body cavity) in mutant worms. Corresponding bright field images are shown in panels A, C, E, G. Bar, 20 m.

A higher rate of passive exchange of DHE between lipid membranes compared to cholesterol could affect the kinetics of DHE trafficking between cellular membranes in *C. elegans* (40,41). Spontaneous transfer of DHE between lipid membranes in the fluid phase has been measured to be about five times faster than that of cholesterol, though rates for protein-mediated transfer seem to be comparable (40–42). The steady-state distribution of DHE and natural sterols like cholesterol or ergosterol in nematodes should be comparable, since (i) DHE shows the same partition preference as cholesterol in lipid membranes of varying composition (14,43–45) and (ii) a non-transferable pool of comparable size has been detected for both sterols in liposomes (40,41). Thus, the kinetics of sterol exchange might be different, but the steady-state distribution of DHE and cholesterol or ergosterol should be comparable. We made sure to study DHE's steady-state distribution in the worms by choosing a long labelling protocol of 1–3 days (see *Materials and methods*).

We demonstrate here that bleach-rate-based image segmentation, combined with RNAi, has the potential for identifying target genes being involved in sterol trafficking and whole-body sterol homeostasis. This is exemplified by silencing the rme-2 gene coding for the yolk receptor which completely blocked import of sterols into oocytes (see Figure 8 and (12)). Our method improves sterol imaging in living *C. elegans* significantly compared to earlier work (12), since it allows us to quantitatively assess in parallel autofluorescence and DHE in a single tissue. Moreover, since autofluorescent, lipofuscin containing gut granule content increases over the life span of *C. elegans*, it is only with our approach that one is able to detect DHE in adult nematodes with sufficient specificity. Our analysis demonstrates that sterol transport to the neuronal and reproductive system in adult *C. elegans* does not require intact intestinal lysosome-like gut granules and does not depend on the function of the ABC-transporter PGP-2, the rab GTPase GLO-1 or its exchange factor GLO-4 (5,6). Lysosomal gut granules might be involved in sterol export from the intestine as suggested by the observed high accumulation of DHE in intestinal storage compartments in glo-mutant but not in wild-type animals (see Figure 6K–N). In fact, a very recent study shows that *C. elegans* can store fats in vesicles that are distinct from Nile Red-stained lysosomes-related organelles (46). We will explore the nature of the sterol-enriched intestinal organelles in glo-mutant worms in the future.

Nematodes possess homologues of enzymes [acylCoA: cholesterol acyltransferase (ACAT) and lecithin:cholesterol acyltransferase (LCAT)] that produce cholesterol esters in mammals, and significant amounts of sterol esters have been detected with radioactive assays in worms (10,19). Kurzchalia and colleagues have shown that about 25% of ^{3}H-photocholesterol associated with vitellogenins gets esterified in *C. elegans* after 2–3 days (12). This quantitiy is similar to what has been reported for esterification of cholesterol in nematodes (19,47). Since we and others demonstrated that DHE is esterified by mammalian ACAT to almost the same extent as cholesterol (48,49), it is likely that some DHE (probably around 20%) gets esterified in *C. elegans* in the time course of our experiment. We showed that esters of DHE, like DHE oleate, have the same fluorescence emission and are indistinguishable from non-esterified DHE when imaged by our UV-sensitive wide field microscope (48). Thus, esterification of DHE in *C. elegans* will not affect the analysis presented in this paper. Studies on DHE metabolism in *C. elegans* with varying genetic background are planned in our laboratory for the future.

Bleach-rate-based image segmentation is suitable to discriminate autofluorescence from probe fluorescence in various applications, specifcally in *in vivo* studies. For example, the neutral lipid stain BODIPY493/503 is very specific for fat-containing gut granules in *C. elegans*, but its emission overlaps with green autofluorescence in the adult nematode (6). Since BODIPY493/503 is a relatively rapidly bleaching stain (50), one might be able to separate its fluorescence from gut granule autofluorescence using our approach. Other applications are the zebrafish *Danio rero*, which has significant autofluorescence in the green channel overlapping with fluorescent probes like fluorescein, BODIPY or nitrobenzoxadiazole (NBD). Here, our method can be used to discriminate autofluorescence from, e.g. NBD-tagged lipids as well as fluorescein-tagged antibodies or dextran. Finally, strongly autofluorescent age pigments impede detection of fluorophores in aging

mammalian nervous tissue (51–53). Here, bleach-rate-based image segmentation could be of use to study structural alterations during aging. This presents again a simple and fast alternative to fluorescence lifetime imaging.

Materials and Methods

Caenorhabditis elegans strains

Maintenance of the strains was according to (54). The wild-type strain used was the strain named N2 Bristol (referred to as N2 or wild type). The mutant strains used were *glo-1(*zu391)X, *glo-4*(ok623)V and *pgp-2*(gk114)I, and maintained on nematode growth medium (NGM) agar plates seeded with the *E. coli* strain OP50 as a food source. OP50 is an uracil auxotroph and its growth is limited on agar and therefore provides nutrients for the worms without overgrowing them (54).

Labelling of nematodes with DHE

A stock solution of DHE (5 mM, from SIGMA Aldrich Chemical was made in ethanol and stored under nitrogen at −80°C. A complex of DHE with methyl-β-cyclodextrin (DHE/MCD) was generated as described (17,55). Two approaches were followed to stain worms with the fluorescent sterol. First, a volume of 20 L of the DHE/MCD solution was added onto the a 24-well agar plate containing bacteria (*E. coli*, strain OP50), and worms were transferred to these plates, incubated for 1–3 days at 20°C and observed by fluorescence microscopy as described below. Second, a protocol developed by Matyash et al. was used to generate a mixture of DHE with bacteria (12). Briefly, an overnight culture of the same bacterial strain was mixed with an equal volume of DHE (5 mM in ethanol), incubated for 30 min at room temperature, and dialysed two times against water. The mixture was incubated with live OP50 bacteria in a ratio 1:5, spread on agar plates and incubated over night to allow for growth of bacteria exactly as reported (12).

RNA interference

For the RNAi experiments, worms were grown on NGM plates not containing cholesterol. All RNAi experiments were performed using RNAi by feeding (56). RNAi clones (rme-2, locus T11F8.3 on chromosome IV, ncr-1, locus F02E8.6 on chromosome X and ncr-2, locus F09G8.4 on chromosome III) were obtained from a library of *E. coli* bacteria [strain HT115(DE3)] transformed with genomic fragments cloned into L4440. This bacteria culture was then seeded on to RNAi agar plates (NGM plates containing 25 g/mL carbenicillin and 1mM IPTG) prepared without adding cholesterol (56). Synchronized L4 worms, grown on NGM plates not containing cholesterol but with DHE added, were washed in M9 buffer (3 g KH_2PO_4, 6g Na_2HPO_4, 5g NaCl, 1 mL 1M $MgSO_4$, H_2O to 1 L) three times to remove remnants of *E. coli* OP50, and transferred to the RNAi plates. From a DHE/MCD solution 200 l were added to the plates kept at 20°C until the worms laid their eggs onto the plates. The parent adult worms were removed and the eggs were left at 20°C until young worms hatched and had at least endured the first larval stage or become adult nematodes. These worms were transferred to microscope slides and sedated with 1M tetrahydromisole in M9 buffer on agar pads just before slides were covered with a coverslip and imaged as described below. As a negative control, worms feeding on bacteria carrying the empty vector L4440 were used and as a positive visual control, RNAi against dpy-13 was used, since dumpy (dpy) worms are shorter and stouter than wild-type worms and therefore easier to detect visually (57).

Wide field epifluorescence microscopy

Wide field fluorescence microscopy and digital image acquisition were carried out using a Leica DMIRBE microscope with a 63 × 1.4 NA oil immersion objective (Leica Lasertechnik GmbH) equipped with a Orca BT512 4-stage peltier and water cooled (−80°C) charge coupled device (CCD) camera (Hamamatsu Photonics Inc.) and a Lambda SC smartshutter (Sutter Instrument Company), driven by ImagePro Plus and ScopePro (Media Cybernetics, Inc.) was used. Optical components and excitation source were described previously (58). DHE in its monomeric form was imaged in the UV using a specially designed filter cube obtained from Chroma Technology Corp with 335-nm (20-nm bandpass) excitation filter, 365-nm dichromatic mirror and 405-nm (40-nm bandpass) emission filter. Differential interference contrast (DIC) imaging was performed on a wide field microscope as described above using DIC optics. DHE-stained or on-stained worms were imaged by repeated acquisition (typically 20 to 30 planes) with an acquisition time of 250–700 ms and no lag time between the acquisitions. To correct for movement of the worms during acquisition the TurboReg or StackReg plugins of ImageJ software were applied (59). Hereby, a rigid body transformation was used to spatially register corresponding planes of DHE (22).

Image segmentation based on bleaching kinetics of DHE in C. elegans

Four different methods were used to visualize sterols selectively based on the rapid bleaching of the DHE in our UV-sensitive wide field microscope compared to cellular autofluorescence in *C. elegans*.

(i) *Pixel-wise least square fitting of mathematical decay models to bleaching kinetics:* Fluorophore containing structures can be revealed by locally analysing the decay rate of the fluorescence emission. In order to study the photobleaching decay, we developed PixBleach, an image-analysis tool which fits a temporal model for each pixels of the field of view. The tool is written as Java plugin to the popular ImageJ image-processing software package (ImageJ: National Institutes of Health, Bethesda, MD, USA, http://rsbweb.nih.gov/ij/). More specifically, we have chosen to implement three common decay models, but PixBleach is designed for easy implementation of other decay models.

(1) The mono-exponential model (m_{mo}):

$$m_{mo}(t) = A \cdot e^{\frac{-t}{\tau}} + B \tag{2}$$

This model contains three parameters to optimize: B the background level, A the amplitude and τ the time constant of the exponential which characterizes the lifetime of the fluorophore in the structure.

(2) The stretched-exponential model (m_{st}):

$$m_{st}(t) = A \cdot e^{\left(\frac{-t}{\tau}\right)^{\frac{1}{h}}} + B \tag{3}$$

This model has four parameters to optimize: B the background level, A the amplitude, τ the time constant and h the heterogeneity factor. The latter parameter can capture the local non-homogeneities of the bleach-time distribution. The stretched-exponential model was proposed by Lee et al. (2001) for analysis of fluorescence lifetime microscopy data, and it yielded increased contrast for FLIM images (23).

(3) The bi-exponential model (m_{bi}):

$$m_{bi}(t) = A_1 \cdot e^{\frac{-t}{\tau_1}} + A_2 \cdot e^{\frac{-t}{\tau_2}} + B \tag{4}$$

This model has five parameters to optimize: B the background level, A_1 and A_2 the amplitudes of the exponentials, τ_1 the short-lived time constant and τ_2 the long-lived time constant.

The fitting of these models to the fluorescence decay data is done by an optimization procedure (Marquart-Levenberg) which tries to minimize the error in the least square sense from the data. Temporal sequences for each pixel are processed independently, in order to create a map for every optimized parameter. To increase the time

performance of the analysis, PixBleach only processes the time-series which have a significant decay from the first frame to the last frame. PixBleach includes also a spatial Gaussian smoothing to de-noise the image and a temporal Gaussian smoothing to compensate residual movements of the sample. PixBleach handles 1000 fittings of time-series in 0.25 s for the mono-exponential model, 0.82 s for the bi-exponential model and 0.86 s for the stretched-exponential model (experimental conditions: Mac 2x2.66 GHz Dual-Core Intel, 4 Gb RAM, time-series of 30 time points, maximum number of iterations: 50). The plugin is available for the biologist community at: http://bigwww.epfl.ch/algorithms/pixbleach.

From the non-linear regression of the models to the decay data and the estimated parameters, the time-integrated fluorescence of DHE was calculated for all models. It is in its analytical form for the mono-exponential model (eqn 2):

$$\begin{aligned}\int_0^n m_{\mathrm{mo}}(t)\mathrm{d}t &= \int_0^n \left(A\cdot e^{\frac{-t}{\tau}} + B\right)\mathrm{d}t \\ &= \left[B\cdot t - A\cdot\tau\cdot e^{\frac{-t}{\tau}}\right]_0^n \\ &= B\cdot n + A\cdot\tau\cdot\left(1 - e^{-n/\tau}\right)\end{aligned} \tag{5}$$

This parameter expresses the total fluorescence emitted by the fluorophore before total photodestruction and is independent of fluorescence quantum yield (25). The integration limit, n, resembles the frame number until which images were acquired in our experiments. To obtain the time-integrated intensity (i.e. the total intensity emitted by the fluorophore), we chose n large enough to collect all light emitted by DHE in direction of the detector (see Supporting Information for a plot of time-integrated intensity for various fluorophore bleach-time constants Figure S8).

(ii) *Image subtraction:* Due to the time hierarchy of the bleach rates of DHE versus cellular autofluorescence, it was assumed that fluorescence of DHE was completely abolished before autofluorescence was significantly reduced. This is reasonable, since we found that the bleach rate of autofluorescence was at least – five- to sixfold lower than that of DHE in living *C. elegans*, as determined by method (i) (see above and *Results* section). To assess the statistical differences in intensity patterns of DHE-labelled worms prior and after bleaching, a PCA was performed using the ImageJ plugin 'PCA' written by Dr. Abrámoff (University of Iowa Hospitals and Clinics, Iowa, USA) . The principle of PCA is to consider every pixel of spatially aligned images as a vector, to calculate the mean, variance and covariance between vector components and to perform a variable transformation which results in a set of orthogonal eigenvectors maximizing the data variation along the eigenvectors of the covariance matrix (see e.g. (58)).

(iii) *Bleach-rate ratio imaging:* Two images were acquired without interval for worms labelled with DHE. For two consecutive images $I_1(x, y)$ and $I_2(x, y)$, the ratio image (I_{bleach}) was calculated which is – in case of a single-exponential bleaching process – related to the bleach rate according to (24,58):

$$\begin{aligned}I_{\mathrm{bleach}}(x, y) &= \exp(E\cdot k(x, y)\cdot t_{\mathrm{d}}) \\ &= \frac{I_1(x, y) - I_\infty(x, y)}{I_2(x, y) - I_\infty(x, y)} \approx \frac{I_1(x, y)}{I_2(x, y)}\end{aligned} \tag{6}$$

Here, I_{bleach} is the bleach-rate image; E is the time and space invariant illumination intensity, k is the bleach-rate constant, t_{d} is a delay time and I_∞ is the intensity in the last image of a bleach experiment. Since this intensity is almost zero for DHE-labelled worms, the approximation in eqn 6 is valid (58). Brackets indicate pixel coordinates x, y for individual image planes. From eqn 6, it becomes clear that in the bleach-rate image only the pixel-dependent bleach rate is a contrast parameter. The method allows therefore to detect local differences in bleach rates of a fluorophore in a living cell or organism (24,58).

(iv) Standard deviation of bleach-rate stacks: Using the z-projection tool in ImageJ, the standard deviation of decaying pixel intensities along the bleach stack was calculated. The resulting standard deviation (STD) image expresses the square root of the intensity variance for each pixel position x, y along the bleach stack:

$$\mathrm{STD}(x, y) = \sqrt{\sigma(x, y)} = \sqrt{\sum_{i=1}^{n}\left(I_i(x, y) - \langle I(x, y)\rangle\right)^2 \Big/ n - 1} \tag{7}$$

where $< I(x, y)>$ describes the mean intensity for pixel x, y for the whole stack, $I_i(x, y)$ is the intensity at pixel position x, y for frame i, and n is the total number of frames. The various methods (i–iv) for bleach-rate-based image segmentation were tested thoroughly on DHE-labelled worms and on simulated images with known bleach rates (see *Results* section) as well as on GUV consisting of DPPC and 45 mol% DHE, prepared as described previously (14).

Three-photon fluorescence microscopy of DHE in living C. elegans

Three-photon excitation fluorescence microscopy measurements of DHE were done using a custom-built microscope. This setup was constructed around an Olympus IX70 microscope. The objective used was a 60× water immersion objective with a NA of 1.2. The excitation light source was a femtosecond Ti:Sa laser (Broadband Mai Tai XF W25 with a 10 W Millennia pump laser, tunable excitation range 710–980 nm, Spectra Physics, Mountain View, CA) and the excitation wavelength used was 930 nm and was circular polarized. For DHE measurements the fluorescence signal was collected using a bandpass filters of 377 ± 25 nm (BrightLine HC). The light was detected by a photo multiplier tube (Hamamatsu H7422P-40) operated in photon counting mode. The data was acquired using simFCS software developed by the Laboratory for Fluorescence Dynamics University of California, Irvine.

Acknowledgments

Daniel Wüstner acknowledges funding by grants of the Danish Heart Association Hjerteforeningen, the Diabetes Foundation Diabetesforeningen as well as the Danish Research Agency Forskningsstyrelsen, Forskningsrådet for Natur og Univers (FNU). Special thanks goes to Dr Greg Herrmann (Department of Biology, Lewis and Clark College, Portland, OR, USA) who kindly provided the *glo*-mutant strains.

References

1. Linsel-Nitschke P, Tall AR. HDL as a target in the treatment of artherosclerotic cardiovascular disease. Nat Rev Drug Disc 2005;4:193–205.
2. Maxfield FR, Tabas I. Role of cholesterol and lipid organization in disease. Nature 2005;438:612–621.
3. Ashrafi K, Chang FY, Watts JL, Fraser AG, Kamath RS, Ahringer J, Ruvkun G. Genome-wide RNAi analysis of Caenorhabditis elegans fat regulatory genes. Nature 2003;421:268–272.
4. Schlegel A, Stainier DY. Lessons from ''lower'' organisms: what worms, flies, and zebrafish can teach us about human energy metabolism. PLoS Genet. 2007;3:e199.
5. Hermann GJ, Schroeder LK, Hieb CA, Kershner AM, Rabbitts BM, Fonarev P, Grant BD, Priess JR. Genetic analysis of lysosomal trafficking in Caenorhabditis elegans. Mol Biol Cell 2005;16: 3273–3288.
6. Schroeder LK, Kremer S, Kramer MJ, Currie E, Kwan E, Watts JL, Lawrenson AL, Hermann GJ. Function of the Caenorhabditis elegans ABC transporter PGP-2 in the biogenesis of a lysosome-related fat storage organelle. Mol Biol Cell 2007;18:995–1008.
7. Li J, Brown G, Ailion M, Lee S, Thomas JH. NCR-1 and NCR-2, the C. elegans homologs of the human Niemann-Pick type C1 disease

protein, function upstream of DAF-9 in the dauer formation pathways. Development 2004;131:5741–5752.
8. Smith MM, Levitan DJ. Human NPC1L1 and NPC1 can functionally substitute for the ncr genes to promote reproductive development in C. elegans. Biochim Biophys Acta 2007;1770:1345–1351.
9. Sym M, Basson M, Johnson C. A model for niemann-pick type C disease in the nematode Caenorhabditis elegans. Curr Biol 2000;10:527–530.
10. Entchev EV, Kurzchalia TV. Requirement of sterols in the life cycle of the nematode Caenorhabditis elegans. Semin Cell Dev Biol 2005;16:175–182.
11. Merris M, Wadsworth WG, Khamrai U, Bittman R, Chitwood DJ, Lenard J. Sterol effects and sites of sterol accumulation in Caenorhabditis elegans: developmental requirement for 4alpha-methyl sterols. J Lipid Res 2003;44:172–181.
12. Matyash V, Geier C, Henske A, Mukherjee S, Hirsh D, Thiele C, Grant B, Maxfield FR, Kurzchalia TV. Distribution and transport of cholesterol in Caenorhabditis elegans. Mol Biol Cell 2001;12: 1725–1736.
13. Wüstner D. Fluorescent sterols as tools in membrane biophysics and cell biology. Chem Phys Lipids 2007;146:1–25.
14. Garvik O, Benediktsen P, Ipsen JH, Simonsen AC, Wüstner D. The fluorescent cholesterol analog dehydroergosterol induces liquid-ordered domains in model membranes. Chem Phys Lipids 2008;159:114–118.
15. McIntosh AL, Atshaves BP, Huang H, Gallegos AM, Kier AB, Schroeder F. Fluorescence techniques using dehydroergosterol to study cholesterol trafficking. Lipids 2008;43:1185–1208.
16. Mondal M, Mesmin B, Mukherjee S, Maxfield FR. Sterols are mainly in the cytoplasmic leaflet of the plasma membrane and the endocytic recycling compartment in CHO cells. Mol Biol Cell 2009;20:581–588.
17. Hao M, Lin SX, Karylowski OJ, Wüstner D, McGraw TE, Maxfield FR. Vesicular and non-vesicular sterol transport in living cells. The endocytic recycling compartment is a major sterol storage organelle. J Biol Chem 2002;277:609–617.
18. Kurzchalia TV, Ward S. Why do worms need cholesterol? Nat Cell Biol 2003;5:684–688.
19. Chitwood DJ. Biochemistry and function of nematode steroids. Crit Rev Biochem Mol Biol 1999;34:273–284.
20. Gerstbrein B, Stamatas G, Kollias N, Driscoll M. In vivo spectrofluorimetry reveals endogenous biomarkers that report healthspan and dietary restriction in Caenorhabditis elegans. Aging Cell 2005;4:127–137.
21. Wüstner D. Improved visualization and quantitative analysis of fluorescent membrane sterol in polarized hepatic cells. J Microsc 2005;220:47–64.
22. Wüstner D, Færgeman NJ. Chromatic aberration correction and deconvolution for UV sensitive imaging of fluorescent sterols in cytoplasmic lipid droplets. Cytometry A 2008;73:727–744.
23. Lee KC, Siegel J, Webb SE, Lévêque-Fort S, Cole MJ, Jones R, Dowling K, Lever MJ, French PM. Application of the stretched exponential function to fluorescence lifetime imaging. Biophys J 2001;81:1265–1274.
24. Brakenhoff GJ, Visscher K, Gijsbers EJ. Fluorescence bleach rate imaging. J Microsc 1994;175:154–161.
25. Hirschfeld T. Quantum efficiency independence of the time integrated emission from a fluorescent molecule. Applied Optics 1976;15:3135–3139.
26. Benson DM, Bryan J, Plant AL, Gotto AMJ, Smith LC. Digital imaging fluorescence microscopy: spatial heterogeneity of photobleaching rate constants in individual cells. J Cell Biol 1985;100:1309–1323.
27. Schroeder F, Barenholz Y, Gratton E, Thompson TE. A fluorescence study of dehydroergosterol in phosphatidylcholine bilayer vesicles. Biochemistry 1987;26:2441–2448.
28. Frolov A, Petrescu A, Atshaves BP, So PT, Gratton E, Serrero G, Schroeder F. High density lipoprotein-mediated cholesterol uptake and targeting to lipid droplets in intact L-cell fibroblasts. J Biol Chem 2000;275:12769–12780.
29. McIntosh AL, Gallegos AM, Atshaves BP, Storey SM, Kannoju D, Schroeder F. Fluorescence and multiphoton imaging resolve unique structural forms of sterol in membranes of living cells. J Biol Chem 2003;278:6384–6403.
30. Zhang W, McIntosh AL, Xu H, Wu D, Gruninger T, Atshaves B, Liu JC, Schroeder F. Structural analysis of sterol distributions in the plasma membrane of living cells. Biochemistry 2005;44:2864–2884.
31. Zipfel WR, Williams, RM, Webb, WW. Nonlinear magic: multiphoton microscopy in the biosciences. Nat Biotechnol 2003;21:1369–1377.
32. Gualda EJ, Filippidis G, Voglis G, Mari M, Fotakis C, Tavernarakis N. In vivo imaging of cellular structures in Caenorhabditis elegans by combined TPEF, SHG and THG microscopy. J Microsc 2008;229:141–150.
33. Wüstner D. Intracellular cholesterol transport. In: Ehnholm C, editor. Cellular Lipid Metabolism. Springer press; 2009, pp. 157–190.
34. Ghauharali RI, van Driel R, Brakenhoff GJ. Sturcture-oriented fluorescence photobleaching analysis: a method for double fluorescent labeling studies. J Microsc 1997;185:375–384.
35. Koppel DE, Carlson C, Smilowitz H. Analysis of heterogeneous fluorescence photobleaching by video kinetics imaging: the method of cumulants. J Microsc 1989;155:199–206.
36. Mittag A, Lenz D, Bocsi J, Sack U, Gerstner AO, Tárnok A. Sequential photobleaching of fluorochromes for polychromatic slide-based cytometry. Cytometry A 2006;69:139–141.
37. Smutzer G, Crawford BF, Yeagle PL. Physical properties of the fluorescent sterol probe dehydroergosterol. Biochim et Biophys Acta 1986;862:361–371.
38. Nemecz G, FS. Time-resolved fluorescence investigation of membrane cholesterol heterogeneity and exchange. Biochemistry 1988;27:7740–7749.
39. Chong PL, Thompson TE. Depolarization of dehydroergosterol in phospholipid bilayers. Biochim Biophys Acta 1986;863:53–62.
40. Bar LK, Chong PL, Barenholz Y, Thompson TE. Spontaneous transfer between phospholipid bilayers of dehydroergosterol, a fluorescent cholesterol analog. Biochim Biophys Acta 1989;983:109–112.
41. Bar LK, Barenholz Y, Thompson TE. Fraction of cholesterol undergoing spontaneous exchange between small unilamellar phosphatidylcholine vesicles. Biochemistry 1986;25:6701–6705.
42. Xu Z, Farver W, Kodukula S, Storch J. Regulation of sterol transport between membranes and NPC2. Biochemistry 2008;47:11134–11143.
43. Veatch SL, Keller SL. Separation of liquid phases in giant vesicles of ternary mixtures of phospholipids and cholesterol. Biophys J 2003;85:3074–3083.
44. Veatch SL, Polozov IV, Gawrisch K, Keller SL. Liquid domains in vesicles investigated by NMR and fluorescence microscopy. Biophys J 2004;86:2910–2922.
45. Beattie ME, Veatch SL, Stottrup BL, Keller SL. Sterol structure determines miscibility versus melting transitions in lipid vesicles. Biophys J 2005;89:1760–1768.
46. O'Rourke EJ, Soukas AA, Carr CE, Ruvkun G. C. elegans major fats are stored in vesicles distinct from lysosome-related organelles. Cell Metab 2009;10:430–435.
47. Chitwood DJ, Lusby WR, Lozano R, Thompson MJ, Svoboda JA. Sterol metabolism in the Nematode Caenorhabditis elegans. Lipids 1984;19:500–506.
48. Wüstner D, Mondal M, Tabas I, Maxfield FR. Direct observation of rapid internalization and intracellular transport of sterol by macrophage foam cells. Traffic 2005;6:396–412.
49. Hölttä-Vuori M, Uronen RL, Repakova J, Salonen E, Vattulainen I, Panula P, Li Z, Bittman R, Ikonen E. BODIPY-cholesterol: a new tool to visualize sterol trafficking in living cells and organisms. Traffic 2008;9:1839–1849.
50. Listenberger LL, Brown DA. Fluorescent detection of lipid droplets and associated proteins. Curr Protoc Cell Biol 2007;24.
51. Koistinaho J, Sorvaniemi M, Alho H, Hervonen A. Microspectrofluorometric quantitation of autofluorescent lipopigment in the human sympathetic ganglia. Mech Ageing Dev 1986;37:79–89.
52. Usuku T, Nishi M, Morimoto M, Brewer JA, Muglia LJ, Sugimoto T, Kawata M. Visualization of glucocorticoid receptor in the brain of green fluorescent protein-glucocorticoid receptor knockin mice. Neuroscience 2005;135:1119–1128.
53. Crespi F, Croce AC, Fiorani S, Masala B, Heidbreder C, Bottiroli G. Autofluorescence spectrofluorometry of central nervous system (CNS) neuromediators. Lasers Surg Med 2004;34:39–47.
54. Brenner S. The genetics of Caenorhabditis elegans. Genetics 1974;77:71–94.

55. Wüstner D, Herrmann A, Hao M, Maxfield FR. Rapid nonvesicular transport of sterol between the plasma membrane domains of polarized hepatic cells. J Biol Chem 2002;277:30325–30336.
56. Kamath RS, Ahringer RJ. Genome-wide RNAi screening in Caenorhabditis elegans. Methods 2003;30:313–321.
57. von Mende N, Albert PS, Riddle DL, Bird DM. Dpy-13, a nematode collagen gene that affects body shape. Cell 1988;55:567–576.
58. Wüstner D. Plasma membrane sterol distribution resembles the surface topography of living cells. Mol Biol Cell 2007;18: 211–228.
59. Thevenaz P, Ruttimann UE, Unser E. A pyramid approach to subpixel registration based on intensity. IEEE Transactions on Image Processing 1998;7:27–41.